Research Square

Preprints are preliminary reports that have not undergone peer review.
They should not be considered conclusive, used to inform clinical practice,
or referenced by the media as validated information.

Dynamic topological remodeling underlies assembly of the flagellar protein-export channel complex

Tohru Minamino

minamino.tohru.fbs@osaka-u.ac.jp

The University of Osaka

Miki Kinoshita

The University of Osaka

Akihiro Kawamoto

The University of Osaka

Keiichi Namba

Osaka University https://orcid.org/0000-0003-2911-5875

Article

Keywords:

Posted Date: January 6th, 2026

DOI: https://doi.org/10.21203/rs.3.rs-8450974/v1

License: This work is licensed under a Creative Commons Attribution 4.0 International License.
Read Full License

Additional Declarations: There is **NO** Competing Interest.

Version of Record: A version of this preprint was published at Communications Biology on August 3rd, 2026. See the published version at https://doi.org/10.1038/s42003-026-10745-4.

Abstract

FliP, FliQ, and FliR forms a membrane-embedded channel for flagellar protein export. How these subunits assemble into the functional channel remains unclear. Here we combined topological mapping, cryo-EM image analysis, and biochemical assays to dissect the assembly mechanism of the FliPQR complex. Using PhoA fusion assays, we show that membrane-spanning helices of each subunit are repositioned toward the periplasm upon complex assembly, revealing large-scale topological remodeling. FliP alone exists in a dynamic equilibrium between pentameric and hexameric states, indicating that the sixth FliP subunit associates weakly and dissociates easily. FliR inserts into the gap between the first and fifth FliP subunits, forming a stable FliPR complex. The FliQ-like element in FliR efficiently recruits the first FliQ subunit. These findings uncover a previously unrecognized mechanism by which hierarchical assembly and structural remodeling drive the efficient and robust formation of the flagellar export channel.

Introduction

The bacterial flagellum is a sophisticated nanomachine composed of a basal body, which functions as a rotary motor; a filament, which acts as a helical propeller; and a hook, which functions as a universal joint connecting the basal body and filament. Flagellar structural subunits are transported from the cytoplasm by the flagellar type III secretion system (fT3SS) at the base of the flagellum and assemble at the distal end of the growing flagellar structure. The fT3SS comprises a transmembrane export gate complex and a cytoplasmic ATPase ring complex (Fig. 1a)[1,2]. The export gate complex consists of FlhA, FlhB, FliP, FliQ and FliR and is embedded within the central pore of the basal body MS-ring. It is powered by proton motive force across the cytoplasmic membrane, whereas the cytoplasmic ATPase ring, composed of FliH, FliI, and FliJ, is required for the export gate complex to function as an active proton-protein antiporter that couples inward-directed proton flow with outward-directed protein export.[3,4]

FliP and FliR form a core structure for assembly of the other export gate proteins. Five FliP subunits and one FliR subunit form the $FliP_5FliR_1$ complex (FliPR) with the assistance of FliO[5–7]. Four FliQ subunits then assemble peripherally to generate the $FliP_5FliQ_4FliR_1$ complex (FliPQR). The FliPQR complex adopts a right-handed helical structure with a narrow central pore (Fig. 1b and Supplementary Fig. 1a) and serves as a protein-export channel for the translocation of flagellar structural subunits across the cytoplasmic membrane[8–11].

The FliPQR complex is gated on both the cytoplasmic and periplasmic sides. On the periplasmic side, the N-terminal α1 helices of FliP and FliR form a gate that is completely sealed by a β-cap composed of the N-terminal β-strands of FliP and FliR, until six FliE subunits assemble on top of FliP and FliR to form the first layer of the rod structure[12]. On the cytoplasmic side, the gate is tightly closed by the $FliP_{Gasket}$ loop (residues 208–213, connecting helices α5 and $α6_a$), the $FliQ_{Latch}$ loop (residues 42–50, between helices $α1_b$ and $α2_a$), the $FliR_C$ loop (residues 208–212, connecting helices $α8_a$ and $α9_a$), and the $FliR_{Plug}$ loop (residues 107–123). The $FliP_{Gasket}$ and $FliR_{Plug}$ loops also prevent the leakage of small molecules

during high-speed protein translocation[13,14]. FlhB, in coordination with the cytoplasmic ATPase complex, regulates the dynamic opening and closing of the cytoplasmic gate[15].

FlhB surrounds the FliPQR complex via its N-terminal transmembrane domain[16], followed by the assembly of nine FlhA subunits around the FliPQR-FlhB complex[17–19]. The C-terminal cytoplasmic domains of FlhB and FlhA project into the central cavity of the basal body C-ring[15] and acts as a substrate-docking platform that facilitates substrate entry to the gate and ensures the correct export order of flagellar structural subunits in accord with the assembly order of the flagellum[20–27].

FliP, FliQ, and FliR are predicted from their amino acid sequences to contain four, two, and six transmembrane (TM) helices, respectively (Supplementary Fig. 2) [28,29]. In the FliPQR complex structures solved by high-resolution cryo-electron microscopy (cryo-EM) image analyses, however, these subunits do not adopt canonical membrane topologies; instead, helix-turn-helix motifs allow formation of the right-handed helical structure (Fig. 1b) [8,9]. The predicted TM3 and TM4 helices of FliP, which correspond to helices α5 and α6a, the predicted TM1 and TM2 helices of FliQ, which correspond to helices α1 and α2, and the predicted TM5 and TM6 helices of FliR, which correspond to helices α8 and α9, are embedded within the cytoplasmic membrane during assembly of the FliPQR complex (Fig. 1b, Supplementary Fig. 2, and Supplementary Table 1). In contrast, the predicted TM1 and TM2 helices of FliP and the predicted TM1–TM4 helices of FliR are located within the periplasmic space in the assembled FliPQR complex, raising the possibility that extensive topological remodeling of both FliP and FliR occurs during FliPR complex formation.

To clarify this hypothesis, we investigated the helical assembly mechanism of the FliPQR complex in *Salmonella enterica* serovar Typhimurium (hereafter referred to as *Salmonella*). We analyzed transmembrane topologies of FliP, FliQ, and FliR individually using PhoA fusion proteins. We show that membrane-spanning helices of individual FliP, FliQ, and FliR subunits are repositioned to the periplasm upon complex assembly, indicating large-scale topological remodeling during their assembly. We also examined intermolecular interactions of FliP-FliP, FliP-FliR, and FliP-FliQ by chemical crosslinking, Blue Native PAGE, cryo-EM, and co-purification assay. FliP alone exists in a dynamic equilibrium between pentameric and hexameric states, suggesting that the sixth FliP subunit readily dissociates. In contrast, FliR remains associated with the $FliP_5$ complex, suggesting that FliR tightly inserts between the first and fifth FliP subunits to stabilize the complex. Deletion analysis revealed that the FliQ-like element in FliR is required for stable association of FliR and FliQ with FliP. We propose a hierarchical assembly mechanism in which topological remodeling of FliP, FliQ, and FliR drives precise formation of a right-handed helical architecture of the FliPQR complex with a narrow central pore.

Results

Transmembrane topologies of FliP, FliQ, and FliR in their monomeric states. To clarify how FliP, FliQ, and FliR assemble into the protein-export channel complex, we analyzed their individual membrane

topologies using alkaline phosphatase (PhoA) fusion assays on L-broth agar plate containing a chromogenic substrate of alkaline phosphatase, 5-Bromo-4-chloro-3-indolyl phosphate (BCIP). As controls, we used precursor PhoA (prePhoA), which carries a signal peptide and becomes active in the periplasm, and mature PhoA (mPhoA), which lacks the signal peptide and remains inactive in the cytoplasm.

For FliP, we constructed five FliP-PhoA fusions: $FliP_{(1–21)}$-PhoA (P1), $FliP_{(1–80)}$-PhoA (P2), $FliP_{(1–161)}$-PhoA (P3), $FliP_{(1–208)}$-PhoA (P4), and $FliP_{(1–245)}$-PhoA (P5) (Fig. 2a and Supplementary Fig. 2). The PhoA activity was detected for P1, P3, P4, and P5, but not for P2, indicating that the loop connecting helices α2 and $α3_a$ resides in the cytoplasm. Thus, the α1 helix together with the N-terminal portion of the α2 helix is predicted to constitute TM1, whereas the α3a helix corresponds to TM2, and these helices are likely to act as the transmembrane helices in the monomeric state, positioning both the N- and C-termini of FliP in the periplasm. Furthermore, the $FliP_{Gasket}$ loop, which tightly closes the cytoplasmic gate along with the $FliQ_{Latch}$, $FliR_{Plug}$, and $FliR_C$ loops, is located in the periplasm. Because α1, α2, and $α3_a$ are situated in the periplasm in the assembled FliPQR complex, we propose that each FliP subunit undergoes substantial conformational rearrangement during assembly.

For FliQ, we examined three PhoA fusions: PhoA-FliQ (Q1), $FliQ_{(1–47)}$-PhoA (Q2), and $FliQ_{(1–89)}$-PhoA (Q3) (Fig. 2b and Supplementary Fig. 2). Only Q1 showed the PhoA activity, indicating that the N-terminus of FliQ is in the periplasm, whereas the $FliQ_{Latch}$ loop and the C-terminal α2 helix are in the cytoplasm in the monomeric state. We therefore propose that the interaction of FliQ with the preassembled FliPR complex promotes the insertion of the α2 helix into the cytoplasmic membrane, stabilizing its proper topology in the FliPQR complex.

For FliR, seven PhoA fusions were examined: PhoA-FliR (R1), $FliR_{(1–34)}$-PhoA (R2), $FliR_{(1–64)}$-PhoA (R3), $FliR_{(1–103)}$-PhoA (R4), $FliR_{(1–169)}$-PhoA (R5), $FliR_{(1–206)}$-PhoA (R6), and $FliR_{(1–264)}$-PhoA (R7) (Fig. 2c and Supplementary Fig. 2). The PhoA activity was detected in R3–R6 but not in R1, R2, or R7, indicating that both the N- and C-termini of FliR are located in the cytoplasm, whereas the R_C loop connecting $α8_b$ and $α9_a$ is in the periplasm in the monomeric state. In contrast, within the assembled FliPQR complex, both termini of FliR face the periplasm, and the R_C loop serves as the cytoplasmic gate of the FliPQR complex. These observations suggest that FliR undergoes substantial conformational remodeling upon assembly with FliP.

Taken together, the PhoA fusion assays demonstrate that FliP, FliQ, and FliR adopt substantially different topologies in their monomeric state compared with the assembled FliPQR complex. These findings suggest that large-scale remodeling of their transmembrane helices occurs during stepwise assembly, rather than being fixed at the time of initial membrane insertion.

Oligomeric states of FliP. FliP can assemble into a homo-hexamer when overexpressed in *Salmonella*[6]. To examine its oligomerization pathway, we overexpressed His-FliP in the absence of FliQ and FliR,

solubilized crude membranes with 1.0% (w/v) lauryl maltose neopentyl glycol (LMNG), and purified the protein by Ni-NTA affinity chromatography and size-exclusion chromatography (SEC). Because the F150A and E178A substitutions, located at the subunit-subunit interface, disrupt FliP oligomerization and abolish function[6], we purified these mutant proteins as well (Fig. 3a). When analyzed by Blue Native PAGE, wild-type FliP migrated as two distinct bands corresponding to a pentamer and a hexamer (Fig. 3b). By contrast, both mutant variants lacked these oligomeric bands, indicating that wild-type FliP exists in a dynamic equilibrium between pentameric and hexameric states.

Previous work showed that residues 110–188 of *Thermotoga maritima* FliP forms a tetramer in solution as judged by sedimentation equilibrium analytical ultracentrifugation measurements, although the tetramer partially dissociates into dimers[30]. This raises the possibility that three dimers could assemble into a hexamer. To test this hypothesis, we performed chemical crosslinking with glutaraldehyde to probe the oligomeric distribution of *Salmonella* FliP (Fig. 3c). Crosslinked wild-type FliP samples produced discrete bands corresponding to monomer, dimer, trimer, tetramer, and pentamer, but a clear hexameric band of wild-type FliP was scarcely detected. This suggests that the sixth FliP subunit associates only weakly with the pentamer. In contrast, crosslinked samples of FliP(F150A) and FliP(E178A) yielded bands corresponding to predominantly dimers, with minor monomer and trimer species, and no higher-order oligomers.

Taken together, these results indicate that FliP monomers assemble stepwise into higher-order states. FliP forms both pentamers and hexamers, but the pentameric state appears to be the more stable species, with incorporation of the sixth subunit being relatively unstable.

Structural characterization of the FliP complex by cryo-EM. To investigate how FliP subunits assemble into oligomeric structures, we performed cryo-EM image analysis. A total of 4,297,085 particles were automatically picked from 12,785 micrographs and extracted with a box size of 80 pixels (4× binned) using cryoSPARC[31]. After three rounds of 2D classification, 589,514 particles were selected for initial model generation of the FliP complex in cryoSPARC. However, no correct 3D model could be obtained because of strong preferred particle orientations. Nevertheless, comparison between the 2D class averages of the FliP complex and projection images obtained from EMD-4733 revealed that the FliP hexamer exhibits a helical architecture with a narrow central pore, closely resembling that of the FliPQR complex (Fig. 4 and Supplementary Fig. 3). These observations suggest that FliP-FliP interactions induce substantial topological rearrangements, leading to the formation of a right-handed helical structure.

Stability of the FliPR complex in the absence of FliQ. We found that the sixth FliP subunit readily dissociates from the FliP pentamer, raising the possibility that self-association of FliP initiates assembly of the FliPQR complex, with FliR inserting into the site created between the first and fifth FliP subunits. If this is the case, unlike the sixth FliP subunit, FliR would not dissociate from the FliP pentamer even in the absence of FliQ. To test this hypothesis, we purified the FliPR and FliPQR complexes using the same procedure as for the FliP complex. SEC revealed that FliR stably associates with FliP even without FliQ (Fig. 5a). To confirm this, we performed Blue Native PAGE (Fig. 6a). In contrast to the FliP complex,

which exhibited two distinct bands corresponding to the pentamer and hexamer, the FliPR complex showed a single band corresponding to a heterohexamer with a stoichiometry of five FliP subunits and one FliR subunit. These results indicate that FliR firmly seals and stabilizes this hexameric structure.

To understand why the sixth FliP subunit readily dissociates from the hexamer, we constructed a structural model of the FliP hexamer based on the cryo-EM structure of the FliPQR complex (PDB ID: 9K29) (Fig. 6b and Supplementary Fig. 4). Because both FliP and FliR contain a FliQ-like structural element (Supplementary Fig. 1c, d), we first superimposed FliQ onto FliR with a root-mean-square deviation (RMSD) of 1.255 Å and then superimposed FliP onto FliQ with an RMSD of 1.162 Å. Five FliP subunits were aligned onto FliR with RMSD values ranging from 1.048 to 1.287 Å. The N-terminal region of FliR, which includes helices α1 and α2, forms extensive hydrophobic contacts with the first FliP subunit, whereas the α1 helix of the sixth FliP subunit cannot. Moreover, the N-terminal β1 strand of FliR forms an antiparallel β-sheet with the β-hairpin of the second FliP subunit, while the β-hairpin of the sixth FliP subunit does not. Instead, this N-terminal region of the sixth FliP subunit sterically clashes with the fifth FliP subunit. These structural incompatibilities likely destabilize the interaction of the sixth FliP subunit, leading to its dissociation from the FliP hexamer. Because FliR is a structural fusion of FliP and FliQ (Fig. 5b), it can form these interactions with FliP at the periplasmic side, thereby tightly closing and stabilizing the FliPR complex.

Because the first FliP subunit is positioned at the top of the right-handed helical architecture of the FliPR complex with the remaining four subunits arranged along the helical staircase (Supplementary Fig. 1a), we propose that intermolecular interactions between each newly incorporated subunit and its nearest pre-existing neighbor trigger large topological rearrangements. These rearrangements create the next assembly site and elevate the pre-existing subunits in a clockwise spiral from the cytoplasmic membrane toward the periplasm.

Role of the FliQ-like structural element in FliR in FliPQR complex formation. Four FliQ subunits peripherally associate with the FliPR complex (Supplementary Fig. 1a). The N-terminal α1 and C-terminal α2 helices of the first FliQ subunit interact with the FliQ-like elements of the FliR and first FliP subunits, respectively (Fig. 5b). PhoA fusion experiments indicate that the C-terminal α2 helix is located in the cytoplasm when FliQ exists as a monomer (Fig. 2b), raising the possibility that the interaction of α1 of FliQ with the FliQ-like element in FliR induce a topological rearrangement of FliQ. This rearrangement may allow the α2 helix to insert into the cytoplasmic membrane, enabling it to contact the first FliP subunit. These interactions would stabilize the association of the first FliQ subunit with the FliPR complex, thereby efficiently initiating the assembly of FliQ subunits around the FliPR complex. If this is the case, the FliQ-like element in FliR may be essential for efficient and robust initiation of FliQ assembly.

To test this hypothesis, we purified the His-FliPQ complex by Ni-affinity chromatography. SEC revealed that, unlike the wild-type FliPQR complex, only a small fraction of FliQ co-eluted with FliP (Fig. 5a), indicating that the FliQ-FliR interaction is required for stable association of FliQ with FliP.

To further determine whether the FliQ-like structural element in FliR contributes to stable FliQ association with the FliPR complex, we constructed a *Salmonella fliR* deletion mutant lacking this structural element (Δ167–262). The Δ167–262 mutant exhibited a non-motile phenotype in soft agar (Fig. 7a). Consistently, immunoblotting with a polyclonal anti-FlgD antibody showed that this mutant failed to secrete FlgD, a representative export substrate of the fT3SS, into the culture supernatant (Fig. 7b). These results indicate that the FliQ-like structural element in FliR is essential for flagellar protein export via the fT3SS.

We next examined whether the FliQ-like structural element in FliR is directly required for efficient and stable FliPQR complex formation. Because FliO facilitates efficient FliPR complex formation[5–7], we co-expressed the His–FliPQR(Δ167–262) complex with FliO and purified it by Ni-affinity chromatography. SEC revealed that, unlike the wild-type FliOPQR complex, only very small amounts of FliQ and FliR(Δ167–262) co-eluted with FliO and FliP (Fig. 7c). Because FliR is a structural fusion of FliP and FliQ (Fig. 5b), the deletion interferes with strong hydrophobic interactions between the N-terminal α-helices of FliR with FliP and β-sheet formation between the β1 strand of FliR and the β-hairpin of the second FliP subunit, thereby easily dissociating FliR(Δ167–262) from FliP. Therefore, we propose that the FliQ-like structural element in FliR stabilizes the FliPR complex and efficiently recruits the first FliQ subunit to initiate FliQ assembly around the FliPR complex.

Discussion

In the FliPQR complex, five FliP subunits, four FliQ subunits, and one FliR subunit together form a right-handed helical assembly within the cytoplasmic membrane. However, the molecular mechanism underlying the stepwise formation of this intricate architecture has remained elusive. Our study provides mechanistic insight into how these subunits dynamically remodel their transmembrane helix arrangements in the monomeric forms to build the functional FliPQR protein-export channel complex. By integrating our findings with previous structural and biochemical studies, we propose a hierarchical model of assembly that captures both conserved and unique features of this secretion system (Fig. 8).

A notable finding from the PhoA fusion assays is that FliP, FliQ, and FliR display distinct transmembrane topologies in their monomeric forms compared with those observed in the assembled FliPQR complex (Figs. 1b and 2). In the cryo-EM structures, these subunits share a common helix-turn-helix motif that together generate a right-handed helical configuration within the cytoplasmic membrane (Supplementary Fig. 1) [8–12]. Moreover, our cryo-EM image analysis of the purified FliP complex revealed that the FliP hexamer also adopts a highly helical structure resembling that of the complete FliPQR complex (Fig. 4). These observations suggest that the helical channel architecture emerges through large-scale topological remodeling of the FliP, FliQ, and FliR subunits as they interact with one another. Such dynamic rearrangements challenge the traditional view that transmembrane helices remain static once inserted into the lipid bilayer, and instead indicate that membrane protein topologies can be fluid and dynamic and may only be finalized upon higher-order assembly.

When expressed alone, FliP exists in a dynamic equilibrium between pentameric and hexameric states (Fig. 3), implying that the sixth FliP subunit does not stably associate and that the hexamer readily collapses to the pentamer. In contrast, the FliPR complex forms a stable structure consisting of five FliP subunits and one FliR subunit, and FliR remains tightly bound in this complex (Fig. 6a). These observations indicate that metastable intermediates can accumulate until FliR inserts into the gap between the first and fifth FliP subunits, thereby stabilizing the proper stoichiometry. The deletion of the FliQ-like structural element from FliR disrupts this stability (Fig. 7c), suggesting that this element not only completes the hetero-hexameric FliPR structure but also acts as a structural anchor that allows the periplasmic gate to be efficiently and tightly closed during FliPQR assembly.

Our deletion analyses further revealed that FliR plays a pivotal role in guiding the recruitment of the first FliQ subunit into the FliPR complex (Fig. 7c). This finding is consistent with structural evidence showing that the first FliQ subunit interacts with both the first FliP subunit and the FliQ-like element in FliR within the assembled FliPQR complex (Fig. 5b) [8–12]. We therefore propose that this structural element in FliR serves as a docking platform to nucleate FliQ assembly around the FliPR complex. In this way, FliR functions as a central scaffolding subunit that defines the overall symmetry and stoichiometry of the FliPQR protein-export channel.

Structurally, FliR can be viewed as a fusion of FliP and FliQ, forming analogous interactions with both FliP and adjacent FliQ subunits (Fig. 5b). This dual connectivity likely imparts robustness to the stepwise assembly of the FliPQR complex, with FliR acting as a terminal subunit that replaces the sixth FliP, terminates FliPR assembly, and initiates the incorporation of FliQ. This model offers a clear explanation for the evolutionary conservation of the 5 FliP : 4 FliQ : 1 FliR stoichiometry among bacteria possessing both flagellar and virulence type III secretion systems[9,16].

Together, our findings support a hierarchical assembly pathway for the FliPQR complex: (i) FliP first forms a metastable hexamer that readily collapses into a pentamer; (ii) FliR insertion seals the FliP structure into a stable pentamer, forming the FliPR complex; and (iii) efficient recruitment of the first FliQ subunit is guided by the FliQ-like element in FliR. Each stage involves substantial topological remodeling, in which the addition of a new subunit reshapes the pre-existing framework. This hierarchical and self-correcting mechanism provides a means for the system to ensure fidelity during assembly while preventing the accumulation of non-productive intermediates (Fig. 8).

Beyond the FliPQR complex, these results illuminate a general principle for the assembly of membrane-embedded secretion channels. Given that the type III secretion systems of both injectisomes and flagella share a conserved core architecture[32–34], similar remodeling-driven, hierarchical mechanisms may also underlie injectisome assembly. More broadly, our study illustrates that dynamic topological rearrangements of transmembrane helices may represent a universal strategy for constructing complex multi-pass membrane assemblies with high precision.

Methods

Bacterial strains, plasmids, and DNA manipulations. Bacterial strains and plasmids are listed in Supplementary Table 2. DNA manipulations were performed using standard protocols. The cloned DNA fragments were confirmed by DNA sequencing (Eurofins Genomics). BCIP indicator plates contained 1% (w/v) tryptone, 0.5% (w/v) yeast extract, 0.5% (w/v) NaCl, 1.5% (w/v) agar, and 50 μg/ml 5-Bromo-4-chloro-3-indolyl phosphate (BCIP). L-broth contained 1% (w/v) tryptone, 0.5% (w/v) yeast extract, and 0.5% (w/v) NaCl. 2×YT medium contained 1.6% (w/v) tryptone, 1.0% (w/v) yeast extract, 0.5% (w/v) NaCl. Soft tryptone agar plates contained 1% (w/v) tryptone, 0.5% (w/v) NaCl, and 0.35% (w/v) agar. Ampicillin was added as needed at a final concentration of 100 μg ml^{-1}.

PhoA fusion assays. Fresh transformants were inoculated onto BCIP indicator plates containing 100 μg ml^{-1} ampicillin and incubated at 30°C for 18 hours. At least seven independent measurements were performed.

Protein purification. His-FliP, His-FliP(F150A), His-FliP(E178A), His-FliP/HA-FliQ complex, His-FliP/FliR-FLAG complex, His-FliP/HA-FliQ/FliR-FLAG complex, FliO/His-FliP/HA-FliQ/FliR-FLAG complex, and FliO/His-FliP/HA-FliQ/FliR(Δ167–262)-FLAG complex were expressed from pTrc99-based plasmids in *Salmonella* strain SJW1368, in which the *flhDC* master operon required for the expression of all flagellar genes is deleted. Crude membranes were collected by ultracentrifugation and isolated and solubilized with 1% (w/v) LMNG. The solubilized proteins were purified by nickel affinity chromatography, followed by SEC[35].

A 13 ml of the overnight culture of *Salmonella* SJW1368 cells harboring the pTrc99A-based plasmid was added to 1.3 l of 2×YT containing 100 μg ml^{-1} ampicillin. The cells were cultured at 30ºC with shaking until the cell density had reached an OD_{600} of about 0.6. The culture was allowed to stand at 4ºC for 30 minutes and then incubated at 16ºC with shaking for another 24 hours. The cells were harvested by centrifugation (12,000 g, 4ºC, 5 minutes) and stored at -80ºC. The cells were thawed, resuspended in 50 ml of 20 mM Tris-HCl, pH 8.0, 3 mM EDTA and disrupted by sonication. The cell lysates were centrifuged (20,000 g, 4ºC, 10 minutes) to remove cell debris. The supernatants were ultracentrifuged (110,000 g, 4ºC, 1 hour). Harvested membranes were solubilized in 50 mM Tris-HCl, pH 8.0, 300 mM NaCl, 5% (w/v) glycerol, 20 mM imidazole, 1% (w/v) LMNG at 4ºC for 1 h and ultracentrifuged (110.000g, 1h, 4ºC) to remove the insoluble membranes. Solubilized membrane proteins were loaded onto a Ni-NTA agarose column (QIAGEN) and washed extensively with 50 mM Tris-HCl, pH 8.0, 300 mM NaCl, 5% (w/v) glycerol, 20 mM imidazole, and 0.005% (w/v) LMNG. Proteins were eluted with a 100–400 mM imidazole gradient. Fractions containing the protein complex were concentrated, followed by SEC with a Superdex 200 10/300 column (GE Healthcare) equilibrated with 20 mM Tris-HCl, pH 8.0, 300 mM NaCl, 1 mM EDTA, 5%(w/v) glycerol, 0.005% (w/v) LMNG. Fractions were run on sodium dodecyl sulfate-polyacrylamide gel electrophoresis (SDS-PAGE) and then analyzed by Coomassie brilliant blue (CBB) staining and immunoblotting with anti-FliO, anti-FliP, anti-HA, or anti-FLAG antibodies. Immunoblotting was carried out using iBind Flex Western Device as described in the manufacturer's instructions (Thermo Fisher Scientific). Detection was performed with Amersham ECL Prime western blotting detection

reagent (Cytiva). Chemiluminescence signals were captured by a Luminoimage analyzer LAS-3000 (GE Healthcare). All image data were processed with Photoshop software CS6 (Adobe).

Blue Native PAGE. Purified His-FliP, His-FliP(F150A), His-FliP(E178A), His-FliP/FliR-FLAG, and His-FliP/HA-FliQ/FliR-FLAG complexes were run on Native PAGE Novex Bis-Tris gels as described in the manufacturer's instructions (Invitrogen). At least three independent experiments were carried out.

Chemical crosslinking. Purified His-FliP, His-FliP(F150A), and His-FliP(E178A) were dialyzed against 20 mM sodium phosphate, pH 7.0, 100 mM NaCl at 4ºC. Glutaraldehyde was added to 50 µl of each 10 µM protein solution at a final concentration of 0.1% (v/v). After incubation at room temperature for 30 min, Tris was added to quench the reaction at a final concentration of 100 mM, followed by adding 60 µl of 2X SDS loading buffer [125 mM Tris-HCl, pH 6.8, 4% (w/v) sodium dodecyl sulfate (SDS), 20% (w/v) glycerol, 0.002% (w/v) bromophenol blue] containing 1 µl 2-mercaptoethanol. After boiling at 95 ºC for 5 min, proteins in the samples were separated by SDS-PAGE using a 10%–20% gradient polyacrylamide gel, followed by CBB staining. All image data were processed with Photoshop software (Adobe). At least three independent experiments were carried out.

Cryo-EM image processing. A 2.6 µl aliquot of the sample solution was applied to a glow-discharged Quantifoil holey carbon grid (R1.2/1.3, Cu, 300 mesh), blotted for 3.5 s at 4°C, and plunge-frozen into liquid ethane using a Vitrobot Mark IV (Thermo Fisher Scientific). The grids were loaded into a Titan Krios electron microscope (Thermo Fisher Scientific) operated at 300 kV and equipped with a Cs corrector (CEOS GmbH). Images were recorded using a K3 direct electron detector (Gatan) in counting mode, equipped with a GIF energy filter (slit width, 20 eV). Data were automatically collected using SerialEM[36] at a physical pixel size of 0.675 Å, with 96 frames per movie, a dose of 0.52 $e^-/Å^2$ per frame, an exposure time of 1.917 s per movie, and a defocus range of -0.8 to -2.0 µm. In total, 15,901 movies were collected.

The movie frames were aligned for beam-induced motion correction, and the contrast transfer function (CTF) parameters were estimated using cryoSPARC v2.12.4[31]. A total of 4,297,085 particle images were automatically picked from 12,785 micrographs and extracted with a box size of 80 pixels and 4× binning using cryoSPARC. After three rounds of 2D classification, 589,514 particles were selected for initial model generation of the FliP ring using cryoSPARC, but the correct 3D model could not be obtained due to a preferred particle orientation.

To generate 2D projections of the FliPQR complex, we utilized the cryo-EM map EMD-4733 as a reference. The map was loaded into UCSF ChimeraX (version 1.10.1)[37] and oriented along the Z-axis. Using the volume project command, we generated 2D projections of the map along the Z-axis. These projections were inspected and compared to experimental 2D class averages of the FliP complex and the FliPQR complex to evaluate the similarity of structural features.

Structure modeling. We built a structural model of the FliP monomer according to the results obtained from the PhoA fusion assay. We used the first FliP subunit of the FliPQR complex (PDB ID: 9K29) as a

template and made substantial conformational modifications using Coot[38]. First, the α1 and α3 helices were individually straightened at their respective kink regions. Subsequently, taking advantage of the flexibility of the loop between α2 and α3, the orientation of the α3 helix was adjusted to put both α1 and α3 in the transmembrane position, and by using the conformational flexibility of the loop connecting α3 and α4, the remaining C-terminal portion of the protein was then rotated by 180º relative to these two helices to locate it in the periplasm. We also built the model of the FliP homo-hexamer by structural comparison and analysis of FliP subunits in the complex using UCSF ChimeraX (version 1.10.1)[37]. All figures including that of the FliPQR complex (PDB ID: 9K29) were prepared using UCSF ChimeraX[37].

Motility assays in soft agar. Fresh transformants were inoculated into soft agar plates containing 100 μg/ml ampicillin and incubated at 30°C. The assay was performed at least seven times to confirm the reproducibility of the results.

Secretion assay. *Salmonella* cells were grown in 5 ml of L-broth containing ampicillin with shaking at 30ºC until the optical cell density had reached an OD_{600} of 1.4–1.6. Cultures were centrifuged to obtain cell pellets and culture supernatants, separately. The cell pellets were resuspended in SDS loading buffer solution containing 1 μl of 2-mercaptoethanol. Proteins in each culture supernatant were precipitated by 10% trichloroacetic acid and suspended in a Tris/SDS loading buffer (one volume of 1 M Tris and nine volumes of 1 X SDS-loading buffer solution) containing 1 μl of 2-mercaptoethanol. Both whole cellular proteins and culture supernatants were normalized to a cell density of each culture to give a constant number of *Salmonella* cells. After boiling at 95ºC for 3 min, these protein samples were separated by SDS–PAGE and transferred to nitrocellulose membranes using iBlot3 Western Blot Transfer Device (Thermo Fisher Scientific) as described in the manufacturer's instructions. Then, immunoblotting with polyclonal anti-FlgD antibody as the primary antibody and anti-rabbit IgG, HRP-linked whole Ab Donkey as the secondary antibody was carried. At least three independent experiments were carried out.

Statistics and reproducibility. Statistical tests, sample size, and number of biological replicates are reported in the corresponding methods and figure legends.

Declarations

Data availability. All data generated during this study are included in this published article and its Supplementary Information. Strains, plasmids, polyclonal antibodies, and all other data are available from the corresponding author upon request.

Acknowledgements

We thank Kelly T. Hughes for providing the *Salmonella fliR* and *phoN* mutants, Takuma Fukumura for providing the pBAD24E, pKY90, pTrc99CES3, and pTrc99ES plasmids, and Yasuyo Abe for technical assistance. This work was supported in part by JSPS KAKENHI Grant Numbers JP20K15749 and JP22K06162 (to M.K.) and JP19H03182, JP22H02573, and JP22K19274 (to T.M.) and MEXT KAKENHI Grant Numbers JP20H05532, and JP22H04844 (to T.M.). This work has also been supported by

Research Support Project for Life Science and Drug Discovery (BINDS) from AMED under Grant Number JP23am121003, JP24am121003 and JP25am121003 (to K.N.), by the Cyclic Innovation for Clinical Empowerment (CiCLE) from AMED under Grant Number JP17pc0101020 (to K.N.), and by JEOL YOKOGUSHI Research Alliance Laboratories of The University of Osaka (to K.N.).

Author Contributions

K.N. and T.M. conceived and designed research; M.K. and T.M. performed genetic, biochemical, and physiological experiments; M.K., and T.M. analyzed genetic, biochemical, and physiological data; M.K. prepared samples for cryo-EM; A.K. collected and analyzed cryo-EM image data; K.N. and T.M. wrote the paper based on discussion with other authors; M.K. and T.M. created Figures.

Competing interests

The authors declare no competing interests.

References

1. Minamino, T., Kinoshita, M.: Structure, assembly, and function of flagella responsible for bacterial locomotion. EcoSal Plus. **11**, eesp–0011 (2023)
2. Nakamura, S., Minamino, T.: Structure and dynamics of the bacterial flagellar motor complex. Biomolecules. **14**, 1488 (2024)
3. Minamino, T., Kinoshita, M., Morimoto, Y.V., Namba, K.: Activation mechanism of the bacterial flagellar dual-fuel protein export engine. Biophys. Physicobiol. **19**, e190046 (2022)
4. Minamino, T., Kinoshita, M., Namba, K.: Insight into distinct functional roles of the flagellar ATPase complex for flagellar assembly in *Salmonella*. Front. Microbiol. **13**, 864178 (2022)
5. Barker, C.S., Meshcheryakova, I.V., Kostyukova, A.S., Samatey, F.A.: FliO regulation of FliP in the formation of the *Salmonella enterica* flagellum. PLoS Genet. **6**, e1001143 (2010)
6. Fukumura, T., et al.: Assembly and stoichiometry of the core structure of the bacterial flagellar type III export gate complex. PLoS Biol. **15**, e2002281 (2017)
7. Fabiani, F.D., et al.: A flagellum-specific chaperone facilitates assembly of the core type III export apparatus of the bacterial flagellum. PLoS Biol. **15**, e2002267 (2017)
8. Kuhlen, L., et al.: Structure of the core of the type III secretion system export apparatus. Nat. Struct. Mol. Biol. **25**, 583–590 (2018)
9. Johnson, S., Kuhlen, L., Deme, J.C., Abusci, P., Lea, S.M.: The structure of an injectisome export gate demonstrates conservation of the architecture in the core export gate between flagellar and virulence type III secretion systems. mBio. **10**, e00818–e00819 (2019)
10. Johnson, S., et al.: Molecular structure of the intact bacterial flagellar basal body. Nat. Microbiol. **6**, 712–721 (2021)

11. Tan, J., et al.: Structural basis of assembly and torque transmission of the bacterial flagellar motor. Cell. **184**, 2665–2679e19 (2021)
12. Kinoshita, M., et al.: A β-cap on the FliPQR protein-export channel acts as the cap for initial flagellar rod assembly. *Proc. Natl. Acad. Sci. USA* 122, e2507221122 (2025)
13. Ward, E., et al.: Type-III secretion pore formed by flagellar protein FliP. Mol. Microbiol. **107**, 94–103 (2018)
14. Hüsing, S., et al.: Control of membrane barrier during bacterial type-III protein secretion. Nat. Commun. **12**, 3999 (2021)
15. Kinoshita, M., Namba, K., Minamino, T.: A positive charge region of *Salmonella* FliI is required for ATPase formation and efficient flagellar protein export. Commun. Biol. **4**, 464 (2021)
16. Kuhlen, L., et al.: The substrate specificity switch FlhB assembles onto the export gate to regulate type three secretion. Nat. Commun. **11**, 1296 (2020)
17. Abrusci, P., et al.: Architecture of the major component of the type III secretion system export apparatus. Nat. Struct. Mol. Biol. **20**, 99–104 (2013)
18. Morimoto, Y.V., et al.: Assembly and stoichiometry of FliF and FlhA in *Salmonella* flagellar basal body. Mol. Microbiol. **91**, 1214–1226 (2014)
19. Kuhlen, L., Johnson, S., Cao, J., Deme, J.C., Lea, S.M.: Nonameric structures of the cytoplasmic domain of FlhA and SctV in the context of the full-length protein. PLoS One. **16**, e0252800 (2021)
20. Fraser, G.M., et al.: Substrate specificity of type III flagellar protein export in *Salmonella* is controlled by subdomain interactions in FlhB. Mol. Microbiol. **48**, 1043–1057 (2003)
21. Evans, L.D., Poulter, S., Terentjev, E.M., Hughes, C., Fraser, G.M.: A chain mechanism for flagellum growth. Nature. **504**, 287–290 (2013)
22. Bryant, O.J., Dhillon, P., Hughes, C., Fraser, G.M.: Recognition of discrete export signals in early flagellar subunits during bacterial type III secretion. *eLife* 11, e66264 (2022)
23. Qu, D., Jiang, M., Duffin, C., Hughes, K.T., Chevance, F.F.: V. Targeting early proximal-rod component substrate FlgB to FlhB for flagellar-type III secretion in *Salmonella*. PLoS Genet. **18**, e1010313 (2022)
24. Terahara, N., et al.: Insight into structural remodeling of the FlhA ring responsible for bacterial flagellar type III protein export. Sci. Adv. **4**, eaao7054 (2018)
25. Minamino, T., Inoue, Y., Kinoshita, M., Namba, K.: FliK-driven conformational rearrangements of FlhA and FlhB are required for export switching of the flagellar protein export apparatus. J. Bacteriol. **202**, e00637–e00619 (2020)
26. Inoue, Y., et al.: The FlhA linker mediates flagellar protein export switching during flagellar assembly. Commun. Biol. **4**, 646 (2021)
27. Kinoshita, M., Minamino, T., Uchihashi, T., Namba, K.: FliH and FliI help FlhA bring strict order to flagellar protein export in *Salmonella*. Commun. Biol. **7**, 366 (2024)
28. Ohnishi, K., Fan, F., Schoenhals, G.J., Kihara, M., Macnab, R.M.: The FliO, FliP, FliQ, and FliR proteins of *Salmonella typhimurium*: putative components for flagellar assembly. J. Bacteriol. **179**, 6092–6099

(1997)
29. Erhardt, M., et al.: Mechanism of type-III protein secretion: Regulation of FlhA conformation by a functionally critical charged-residue cluster. Mol. Microbiol. **104**, 234–249 (2017)
30. Fukumura, T., et al.: Crystallization and preliminary X-ray analysis of the periplasmic domain of FliP, an integral membrane component of the bacterial flagellar type III protein export apparatus. Acta Crystallogr. Sect. F Struct. Biol. Cryst. Commun. **70**, 1215–1218 (2014)
31. Punjani, A., Rubinstein, J.L., Fleet, D.J., Brubaker, M.A.: cryoSPARC: algorithms for rapid unsupervised cryo-EM structure determination. Nat. Methods. **14**, 290–296 (2017)
32. Wagner, S., et al.: Organization and coordinated assembly of the type III secretion export apparatus. *Proc. Natl. Acad. Sci. USA* 107, 17745–17750 (2010)
33. Dietsche, T., et al.: Structural and functional characterization of the bacterial type III secretion export apparatus. PLoS Pathog. **12**, e1006071 (2016)
34. Zilkenat, S., et al.: Determination of the stoichiometry of the complete bacterial type III secretion needle complex using a combined quantitative proteomic approach. Mol. Cell. Proteom. **15**, 1598–1609 (2016)
35. Kinoshita, M., Namba, K., Minamino, T.: Purification of the transmembrane polypeptide channel complex of the *Salmonella* flagellar type III secretion system. Methods Mol. Biol. **2646**, 3–15 (2023)
36. Mastronarde, D.N.: Automated electron microscope tomography using robust prediction of specimen movements. J. Struct. Biol. **152**, 36–51 (2005)
37. Pettersen, E., et al.: UCSF ChimeraX: Structure visualization for researchers, educators, and developers. Protein Sci. **30**, 70–82 (2021)
38. Emsley, P., Lohkamp, B., Scott, W.G., Cowtan, K.: Features and development of *Coot*. Acta Crystallogr. D Struct. Biol. **66**, 486–501 (2010)

Figures

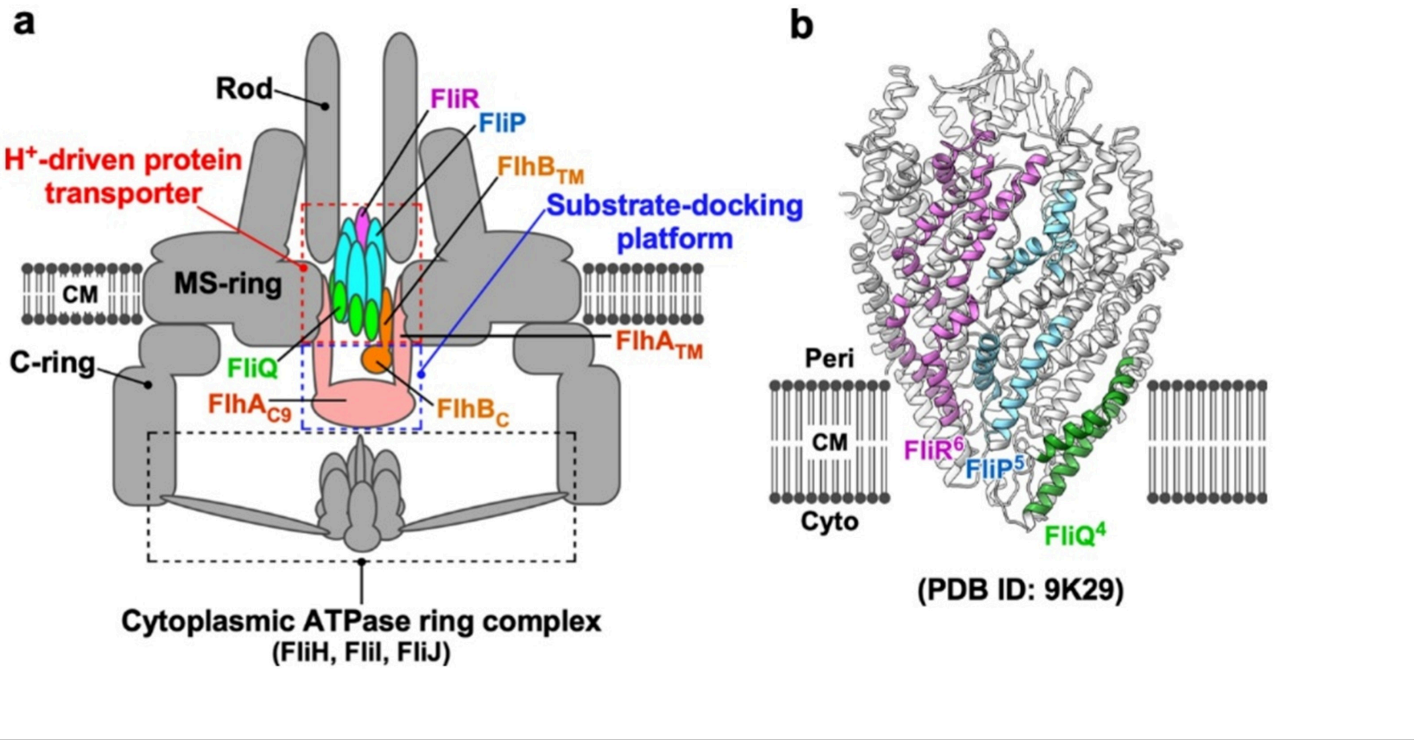

Figure 1

The FliPQR protein-export channel complex of the *Salmonella* flagellar type III secretion system. (a) Schematic diagram of the flagellar type III secretion system. The system is composed of a transmembrane export gate complex with a stoichiometry of nine FlhA subunits, one FlhB subunit, five FliP subunits, four FliQ subunits, and one FliR subunit and a cytoplasmic ATPase ring complex composed of six FliH dimers, six FliI subunits, and one FliJ subunit. The export gate complex resides within the central pore of the basal body MS-ring and functions as a proton (H^+)-protein antiporter that couples inward-directed H^+ flow through the H^+ channel with outward-directed protein translocation through the FliPQR protein-export channel. The cytoplasmic ATPase associates firmly with the basal body C-ring and serves as an ATP-driven activator that enables the export gate complex to operate as an active H^+-driven protein transporter. The C-terminal domains of FlhA and FlhB project into the central cavity of the C-ring and serves as a substrate-docking platform. CM, cytoplasmic membrane. **(b)** Cryo-EM structure of the FliPQR protein-export channel complex (PDB ID: 9K29). The predicted transmembrane (TM) helices of FliP, FliQ and FliR are colored sky blue, forest green, and orchid, respectively (See Supplementary Fig. 2). During assembly of the FliPQR complex, the predicted TM3 and TM4 helices of FliP, the predicted TM5 and TM6 helices of FliR, and the predicted TM1 and TM2 helices of FliQ are embedded within the cytoplasmic membrane whereas the predicted TM1 and TM2 helices of FliP and the predicted TM1–4 helices of FliR are located in the periplasm. Peri, periplasm; Cyto, cytoplasm.

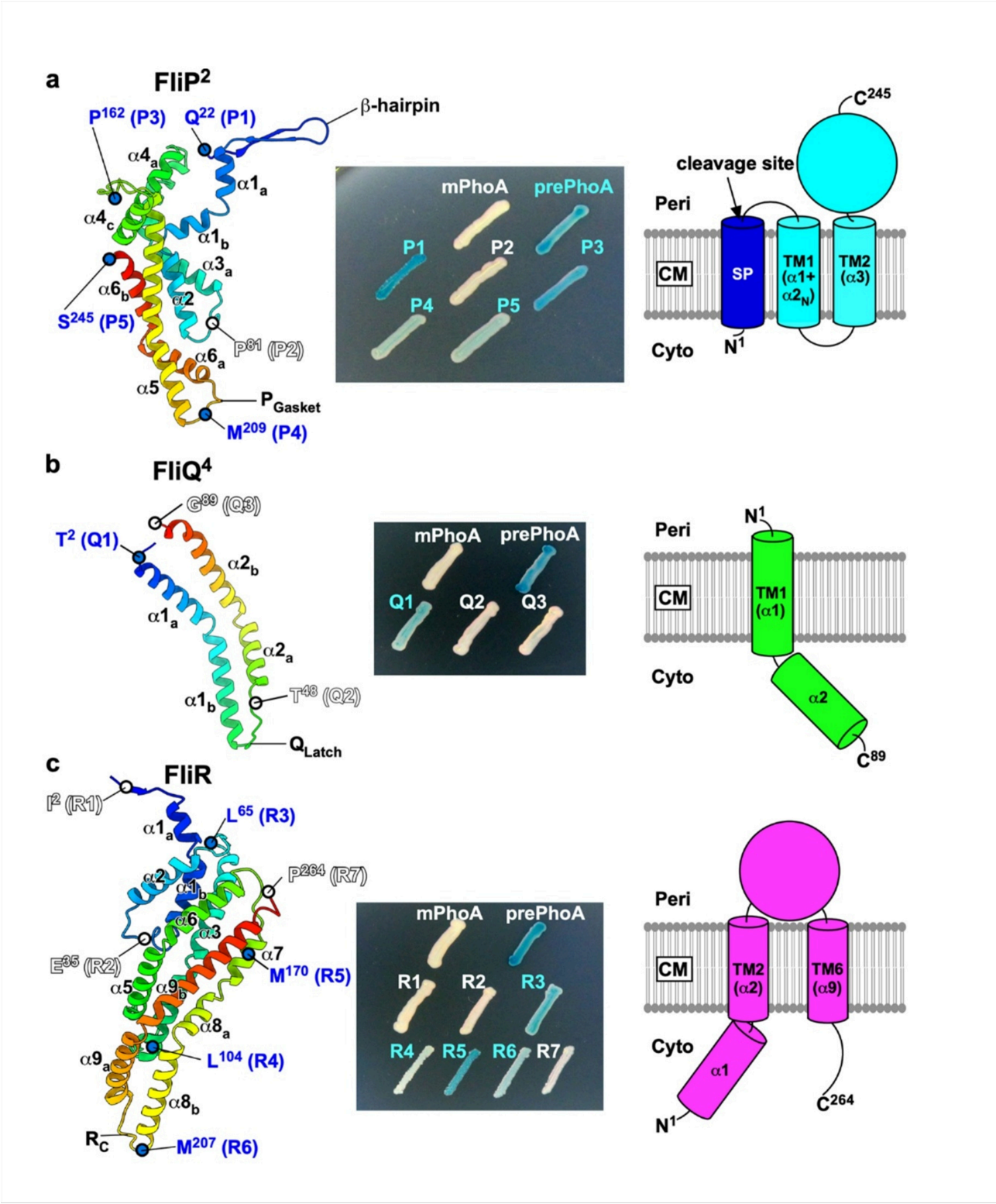

Figure 2

Membrane topology mapping of FliP, FliQ, and FliR. Cα ribbon diagrams of the atomic models of **(a)** the second FliP (FliP^2), **(b)** the fourth FliQ (FliQ^4), and **(c)** FliR subunits are shown (PDB ID: 9K29) (left panel). Five (P1–P5), three (Q1–Q3), and seven (R1–R7) PhoA fusion constructs were generated for FliP, FliQ, and FliR, respectively. The P_{Gasket}, Q_{Latch}, and R_C loops form the cytoplasmic gate of the protein-export channel. PhoA fusion assays for **(a)** FliP, **(b)** FliQ, and **(c)** FliR (middle panels). Fresh *Salmonella*

TH12991 (Δ*phoN*) cells carrying pMKM10001 (pTrc99AFF4/mPhoA), pMKM10002 (pTrc99AFF4/prePhoA), or each PhoA fusion plasmid – pMKM10018 (pTrc99AFF4/FliP$_{(1-21)}$-PhoA, indicated as P1), pMKM10019 (pTrc99AFF4/FliP$_{(1-80)}$-PhoA, indicated as P2), pMKM10020 (pTrc99AFF4/FliP$_{(1-161)}$-PhoA, indicated as P3), pMKM10021 (pTrc99AFF4/FliP$_{(1-208)}$-PhoA, indicated as P4), pMKM10022 (pTrc99FF4A/FliP$_{(1-245)}$-PhoA, indicated as P5), pMKM10003 (pTrc99AFF4/PhoA-FliQ$_{(2-89)}$, indicated as Q1), pMKM10023 (pTrc99AFF4/FliQ$_{(1-47)}$-PhoA, indicated as Q2), pMKM10024 (pTrc99AFF4/FliQ$_{(1-89)}$-PhoA, indicated as Q3), pMKM10025 (pTrc99A/PhoA-FliR$_{(2-264)}$, indicated as R1), pMKM10026 (pTrc99A/ FliR$_{(1-34)}$-PhoA, indicated as R2), pMKM10027 (pTrc99A/FliR$_{(1-64)}$-PhoA, indicated as R3), pMKM10028 (pTrc99A/FliR$_{(1-103)}$-PhoA, indicated as R4), pMKM10029 (pTrc99A/FliR$_{(1-169)}$-PhoA, indicates as R5), pMM10030 (FliR$_{(1-206)}$-PhoA, indicated as R6), or pMM10031 (pTrc99A/FliR$_{(1-264)}$-PhoA, indicates as R7) – were inoculated onto BCIP indicator plates containing 100 μg ml^{-1} ampicillin and incubated at 30°C for 18 hours. In the periplasm, PhoA folds into an active conformation that hydrolyzes BCIP, producing blue colonies on indicator plates. In contrast, PhoA in the cytoplasm remains inactive, resulting in white colonies. Topological models of **(a)** FliP, **(b)** FliQ, and **(c)** FliR monomers are generated based on the PhoA fusion assays (right panels). SP (dark blue cylinder) represents the signal peptide. Spheres represent the remaining parts of FliP and FliR. For FliP, the α1 helix together with the N-terminal portion of the α2 helix (α2$_N$) is predicted to constitute TM1, whereas the α3 helix corresponds to TM2; together, these helices are likely to function as the transmembrane helices in the monomeric state, positioning both the N- and C-termini of FliP in the periplasm. For FliQ, helix α1 is predicted to serve as a transmembrane helix (TM1), and helix α2 is located on the cytoplasmic side in the monomeric state. For FliR, TM2 and TM6, which correspond to helices α2 and α9, respectively, are embedded in the cytoplasmic membrane in the monomeric state, positioning both the N- and C-termini of FliP in the cytoplasm. Peri, periplasmi; CM, cytoplasmic membrane; Cyto, cytoplasm.

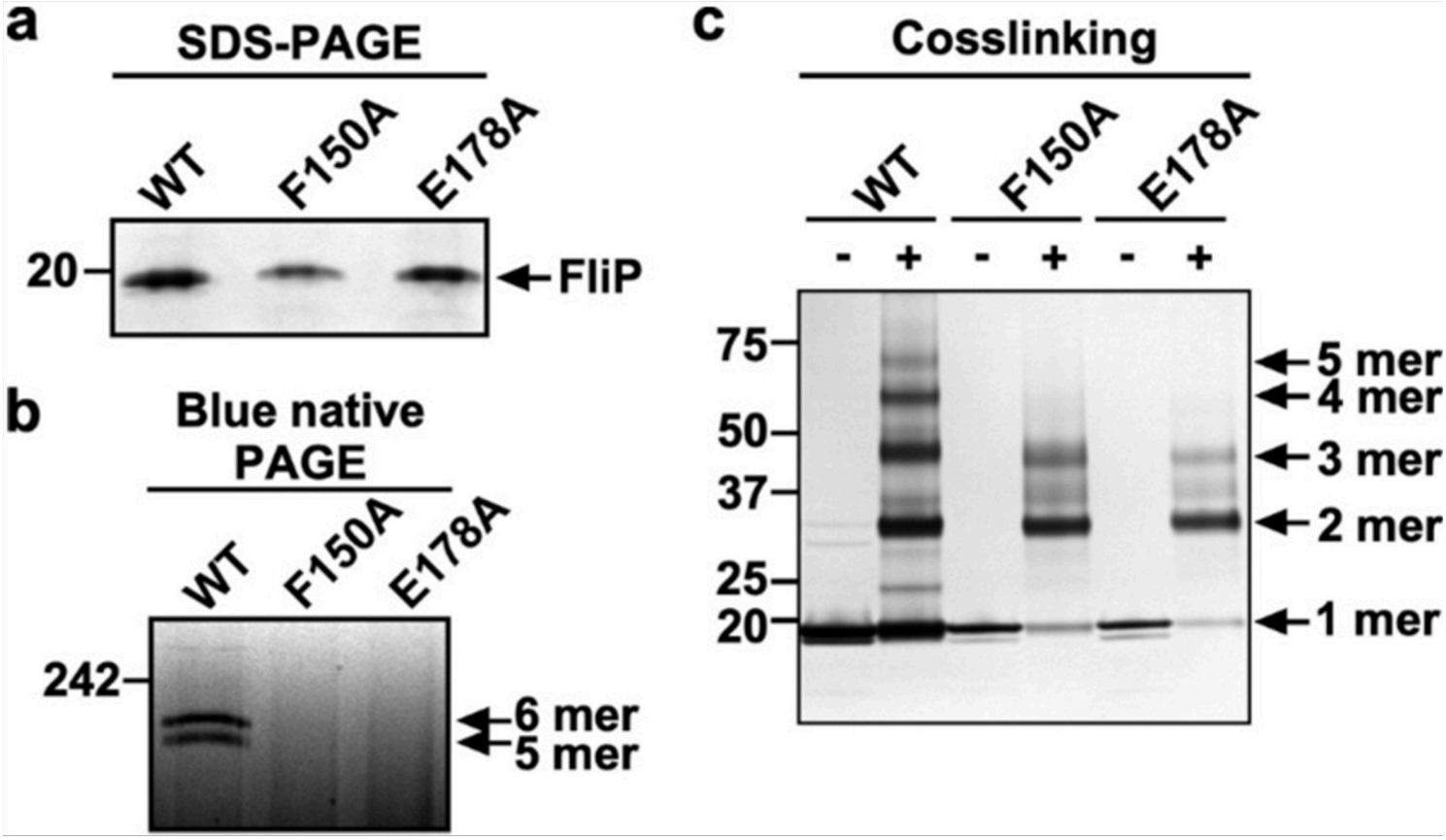

Figure 3

Oligomeric states of FliP. (a) CBB-stained SDS-PAGE gel of purified FliP and its mutant variants, FliP(F150A) and FliP(E178A). **(b)** Blue Native PAGE analysis of purified wild-type FliP and its mutant variants. **(c)** CBB-stained SDS-PAGE gel showing cross-linked products of purified FliP and its mutant variants. The positions of molecular mass markers (kDa) are indicated on the left. At least three independent assays were performed.

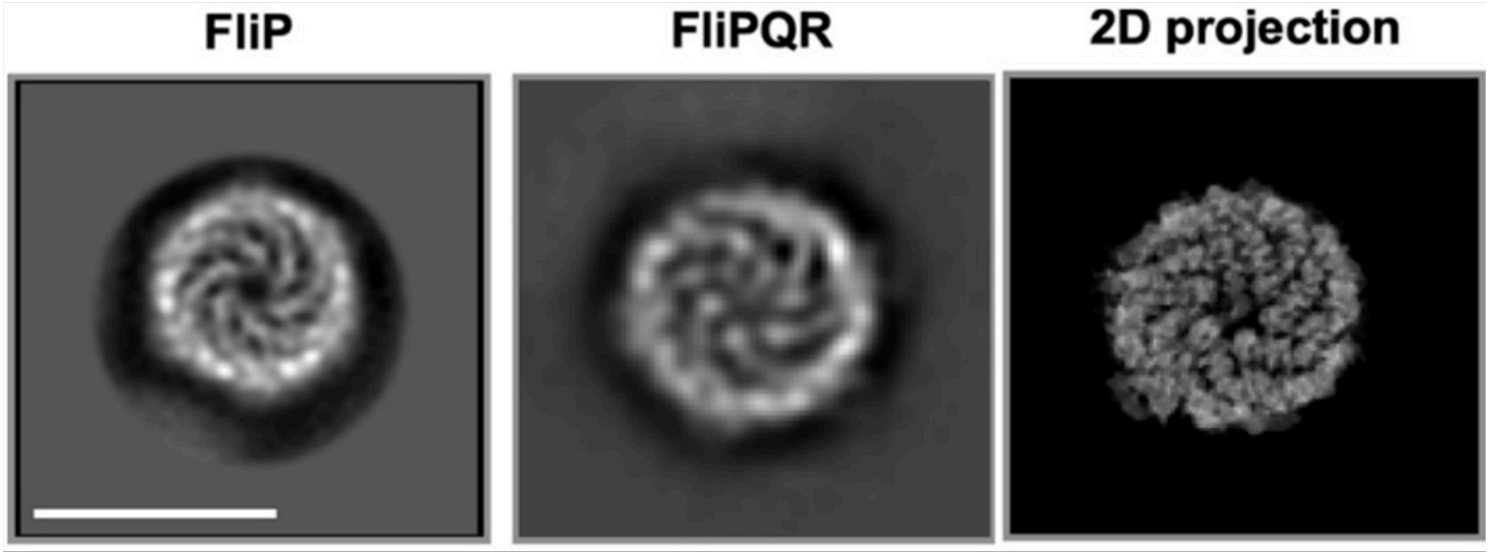

Figure 4

Representative 2D class averages of the FliP complex (left panel) and the FliPQR complex (middle panel) obtained by single particle cryo-EM image analysis and a corresponding model projection image of FliPQR complex (right panel) obtained from EMD-4733 using UCSF ChimeraX. Scale bar, 10 nm.

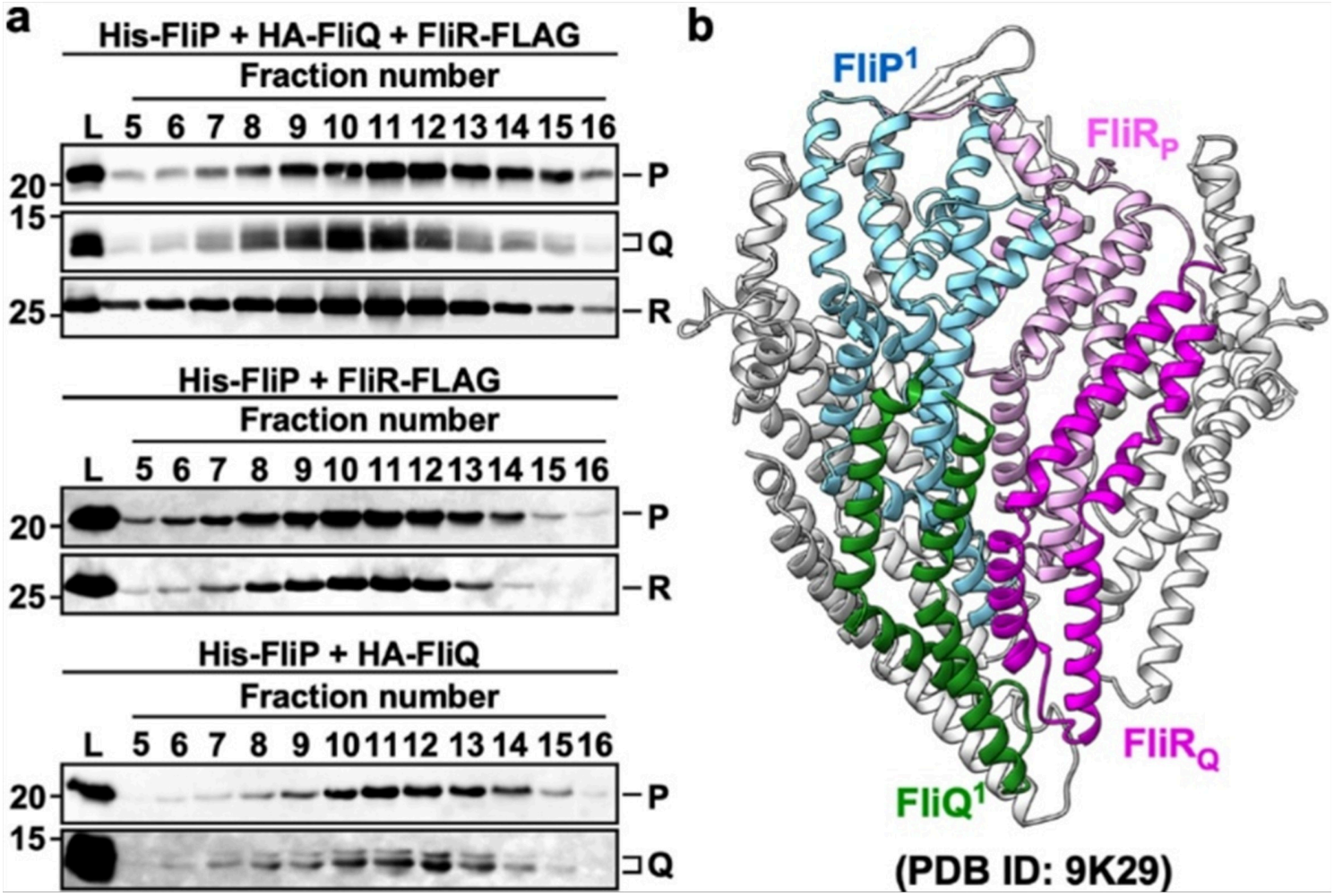

Figure 5

Interactions of FliQ with FliP and FliR. (a) Elution profiles of the His-FliP/HA-FliQ/FliR-FLAG (upper panels), His-FliP/FliR-FLAG, and His-FliP/HA-FliQ complexes from a Superdex 200 10/300 column equilibrated with 20 mM Tris-HCl, pH 8.0, 300 mM NaCl, 1 mM EDTA, 5% (w/v) glycerol and 0.005% (w/v) LMNG. Membrane fractions were solubilized with 1% (w/v) LMNG. Complexes were purified by Ni affinity chromatography, followed by SEC. Immunoblotting of elution fractions were performed using anti-FliP, anti-HA or anti-FLAG antibodies. The positions of molecular mass markers (kDa) are indicated on the left. At least three independent assays were performed. **(b)** Cα ribbon diagram of the atomic model of the FliPQR complex (PDB ID: 9K29). FliR is a structural fusion of FliP ($FliR_P$, plum) and FliQ ($FliR_Q$, magenta). The first FliQ subunit ($FliQ^1$, forest green) associates with the FliQ-like element of FliR and the first FliP subunit ($FliP_1$, sky blue) to initiate FliQ assembly around the FliPR complex.

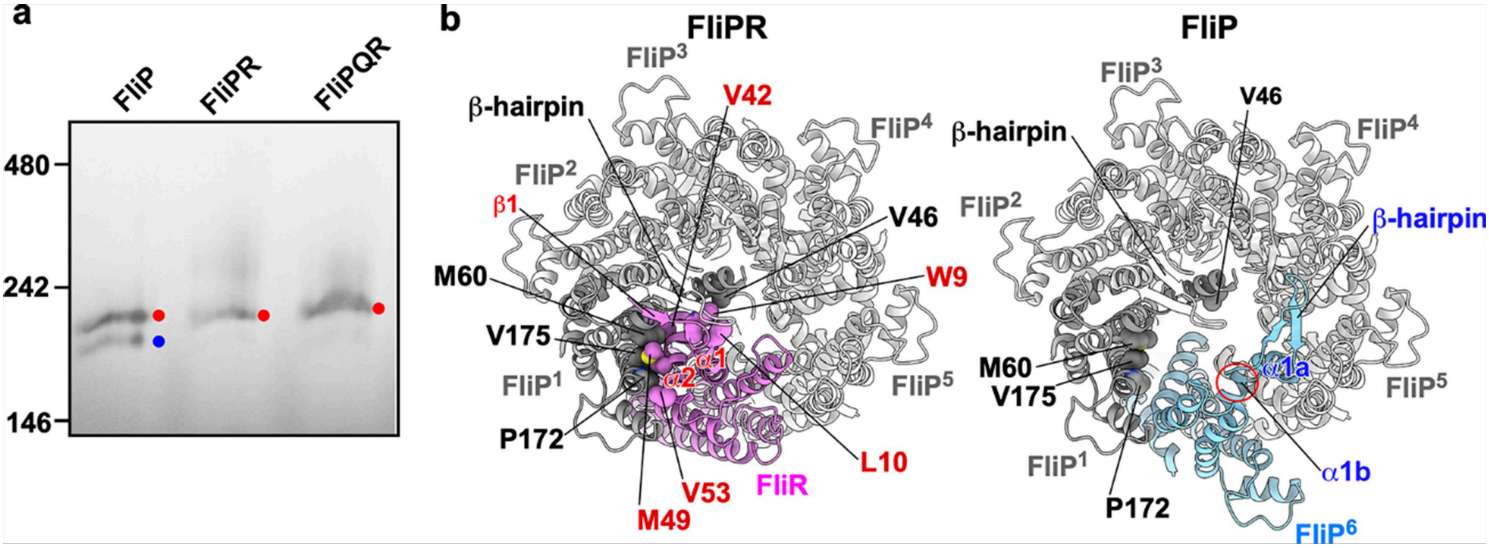

Figure 6

Stability of the FliPR complex. (A) Blue Native PAGE analysis of purified FliP, FliPR and FliPQR complexes. The red dots shown to the right of each lane indicate the positions of the FliP hexamer, the FliPR complex, and the FliPQR complex, whereas the dot shown to the right of the FliP lane indicates the position of the FliP pentamer. The positions of molecular mass markers (kDa) are indicated on the left. **(B)** Model of the FliP homo-hexamer based on the cryo-EM structure of the FliPQR complex (PDB ID: 9K29). FliR was superimposed onto FliQ with root-mean-square deviation (RMSD) of 1.255 Å, and FliP was subsequently superimposed onto FliQ with RMSD of 1.162 Å. Five FliP subunits could be aligned onto FliR with RMSD values ranging from 1.048 to1.287 Å. Among them, the third FliP subunit (P^3) showed the lowest RMSD, indicating the closest structural correspondence. The N-terminal region of FliR (orchid) forms strong hydrophobic contacts with the first FliP subunit (P^1, grey) (left panel) whereas the N-terminal region of the sixth FliP subunit (P^6, sky blue) does not (right panel). The β1 strand of FliR forms an antiparallel β-sheet with the β-hairpin of the second FliP subunit (P^2, light grey) whereas the β-hairpin of $FliP^6$ does not. Furthermore, this N-terminal region sterically clashes with the fifth FliP subunit (P^5), as indicated by the red circle.

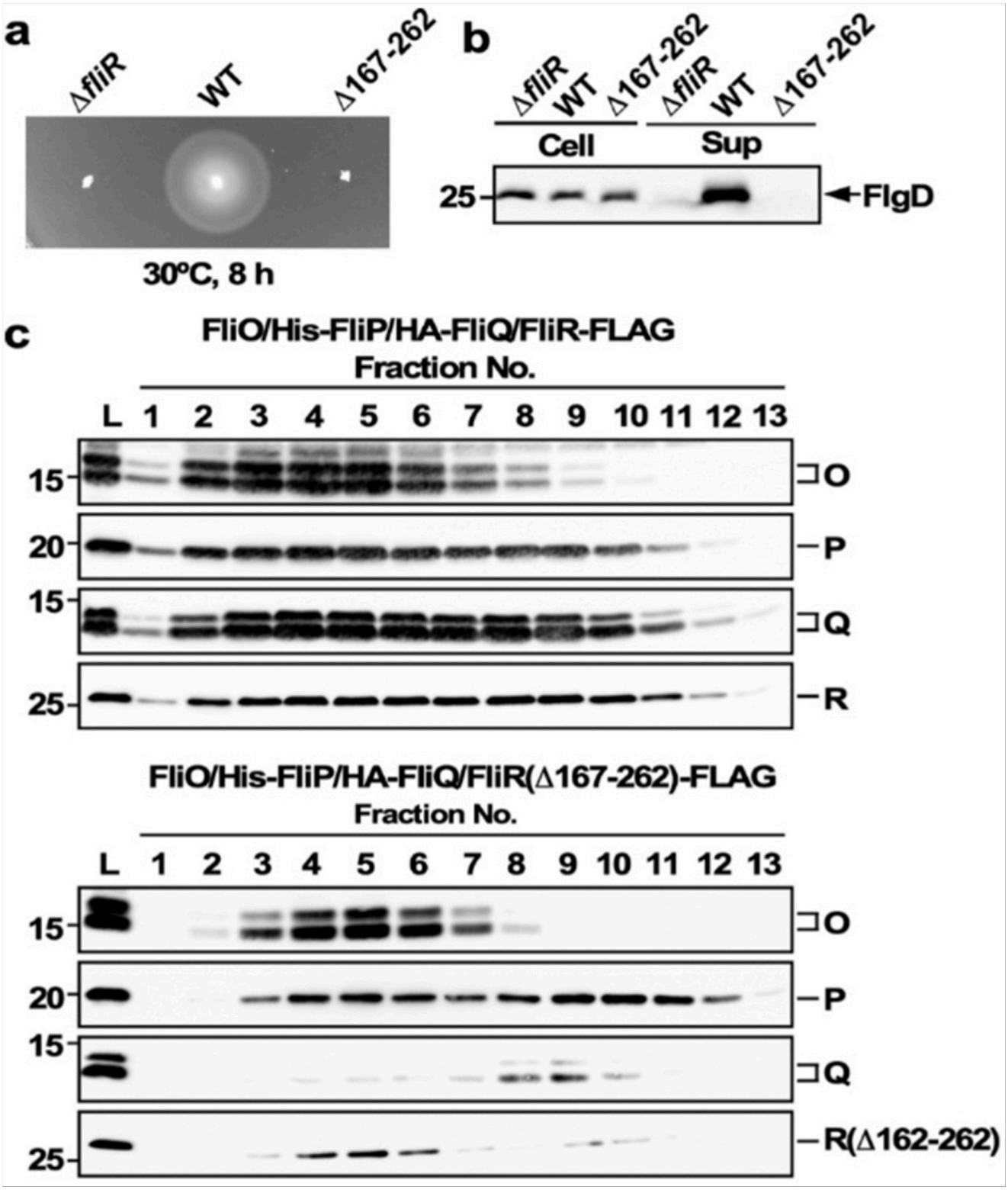

Figure 7

Effect of deletion of the FliQ-like structural element in FliR on flagellar protein export. (a) Motility of a *Salmonella* Δ*fliR*mutant carrying pBAD24E (indicated as Δ*fliR*), pMKM701 (wild-type, WT), or pMKM702 (Δ167-262) in soft agar containing ampicillin and 0.02% (w/v) L-arabinose. Plates were incubated at 30°C for 8 hours. At least seven independent assays were carried out. **(b)** Flagellar protein secretion assays. Whole-cell (Cell) and culture supernatant (Sup) fractions were prepared from the above

transformants. Five microliters of each protein sample, normalized to an optical density at 600 nm, were analyzed by SDS-PAGE followed by immunoblotting with polyclonal anti-FlgD antibody. The position of the 25 kDa molecular mass marker is indicated on the left. At least three independent assays were performed. **(c)** Effect of deletion of the FliQ-like structural element on formation of the FliOPQR complex. Elution profiles of the FliO/His-FliP/HA-FliQ/FliR-FLAG (upper panels) and FliO/His-FliP/HA-FliQ/FliR(Δ167-262)-FLAG complexes from a Superdex 200 10/300 column equilibrated with 20 mM Tris-HCl, pH 8.0, 300 mM NaCl, 1 mM EDTA, 5% (w/v) glycerol and 0.005% (w/v) LMNG. Membrane fractions were solubilized by 1% LMNG. Complexes were purified by Ni affinity chromatography, followed by SEC. Immunoblotting of elution fractions were performed using anti-FliO (1st row), anti-FliP (2nd row), anti-HA (3rd row) or anti-FLAG (4th row) antibodies. The positions of molecular mass markers (kDa) are indicated on the left. At least three independent assays were performed.

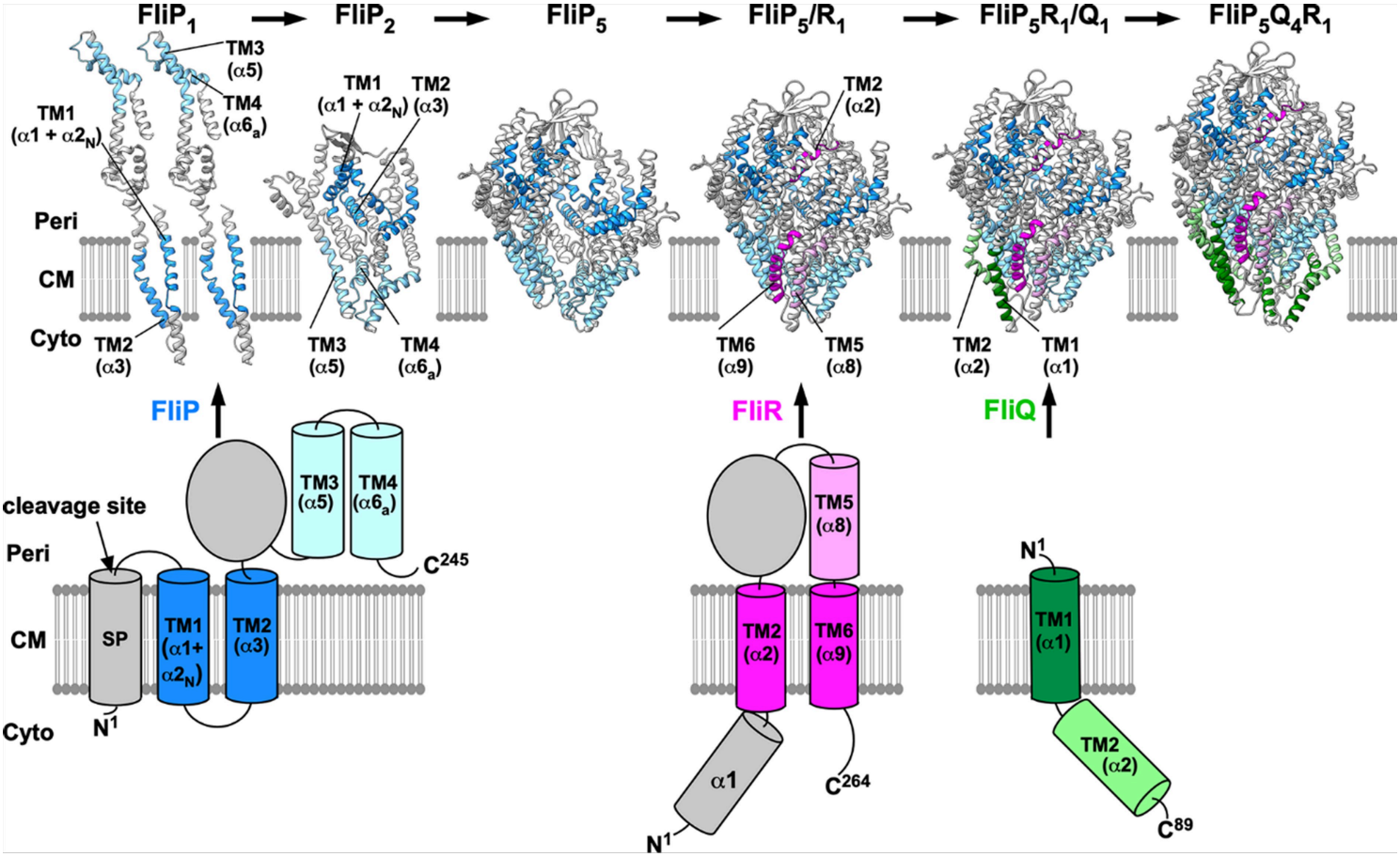

Figure 8

Assembly mechanism of the FliPQR complex. FliP carries a cleavable N-terminal signal peptide, which is removed during membrane insertion. In the monomeric state, the predicted TM1 and TM2 helices of FliP (dodger blue) function as transmembrane helices. Intermolecular FliP-FliP interactions autonomously drive large-scale topological rearrangements within FliP, generating a metastable FliP hexamer that readily collapses into a pentamer ($FliP_5$). As a result of this rearrangement, the predicted TM3 and TM4 helices of FliP (light sky blue) that were located in the periplasm in the monomeric form become transmembrane helices. In the monomeric state of FliR, the predicted TM2 and TM6 helices (magenta)

serves as transmembrane helices. Intermolecular FliP-FliR interactions then induce substantial topological remodeling of FliR, allowing FliR to insert into the gap between the first and fifth FliP subunits to form the $FliP_5R_1$ complex. During this process, the predicted TM6 helix changes its orientation, repositioning the C-terminus toward the periplasm. Together with the predicted TM5 helix (plum), it forms a helix-turn-helix structure that is embedded within the cytoplasmic membrane. The TM1 helix of FliQ (green) interacts with the FliQ-like structural element in FliR, triggering a topological rearrangement of FliQ. This rearrangement allows the α2 helix of FliQ (light green) to contact the first FliP subunit, thereby initiating cooperative assembly of FliQ around the $FliP_5R_1$ complex. All predicted TM helices of each subunit are colored in the ribbon diagrams in the upper panel (See Supplementary Fig. 2).

Supplementary Files

This is a list of supplementary files associated with this preprint. Click to download.

- nrreportingsummary251226.pdf
- KinoshitaSI251226.docx